EXTENDED PDF FORMAT SPONSORED BY
Tools for Your
Biological Target
sigma.com/biotarget2

Mechanism and Kinetics of Spontaneous Nanotube Growth Driven by Screw Dislocations

Stephen A. Morin *et al.*

Science **328**, 476 (2010);
DOI: 10.1126/science.1182977

This copy is for your personal, non-commercial use only.

If you wish to distribute this article to others, you can order high-quality copies for your colleagues, clients, or customers by clicking here.

Permission to republish or repurpose articles or portions of articles can be obtained by following the guidelines here.

The following resources related to this article are available online at www.sciencemag.org (this information is current as of July 12, 2012):

Updated information and services, including high-resolution figures, can be found in the online version of this article at:
http://www.sciencemag.org/content/328/5977/476.full.html

Supporting Online Material can be found at:
http://www.sciencemag.org/content/suppl/2010/04/22/328.5977.476.DC1.html

This article **cites 26 articles**, 6 of which can be accessed free:
http://www.sciencemag.org/content/328/5977/476.full.html#ref-list-1

This article has been **cited by** 1 article(s) on the ISI Web of Science

This article has been **cited by** 1 articles hosted by HighWire Press; see:
http://www.sciencemag.org/content/328/5977/476.full.html#related-urls

This article appears in the following **subject collections:**
Materials Science
http://www.sciencemag.org/cgi/collection/mat_sci

Downloaded from www.sciencemag.org on July 12, 2012

Science (print ISSN 0036-8075; online ISSN 1095-9203) is published weekly, except the last week in December, by the American Association for the Advancement of Science, 1200 New York Avenue NW, Washington, DC 20005. Copyright 2010 by the American Association for the Advancement of Science; all rights reserved. The title *Science* is a registered trademark of AAAS.

pression of a SC gap at the center of vortices may induce Andreev scattering (*16*, *22*, *23*). In both cases, scatterings with sign-preserving momenta should be selectively enhanced, as discussed above. In addition to such $\mathbf{q}$-selective enhancement of QP scatterings, there may be a $\mathbf{q}$-independent overall reduction of QPI intensity under magnetic fields; a Doppler shift of QP energies induced by supercurrent around vortices has been argued to suppress QPI amplitude irrespective of the nature of the scatterings (*16*, *22*, *23*). In total, sign-preserving and sign-reversing scatterings will be enhanced and suppressed, respectively, by a magnetic field. This technique was successfully applied in the detection of the *d*-wave SC-gap function in a cuprate superconductor (*16*).

In the case of $s_\pm$-wave symmetry, $\mathbf{q}_2$ connects Fermi pockets with the opposite sign of the SC gap (sign-reversing scattering), whereas $\mathbf{q}_3$ does Fermi pockets with the same sign (sign-preserving scattering) (Fig. 1A). Therefore, intensities of QPI at $\mathbf{q}_2$ and $\mathbf{q}_3$ should be suppressed and enhanced, respectively, with application of the magnetic field. If the gap symmetry were of a *d*-wave or conventional *s*-wave, the magnetic-field dependence of intensities of QPI at $\mathbf{q}_2$ and $\mathbf{q}_3$ would be qualitatively different from that expected for $s_\pm$-wave symmetry (*13*).

Shown in Fig. 3, C and D, are $Z(\mathbf{r}, E)$ and $Z(\mathbf{q}, E)$, respectively, under a magnetic field of 10 T applied perpendicular to the surface. Both scatterings at $\mathbf{q}_2$ and $\mathbf{q}_3$ show field dependence. In the field-induced change in $Z(\mathbf{q}, E)$ (Fig. 4), an opposite-field dependence is clearly observed between the two scatterings; the intensity at $\mathbf{q}_2$ is suppressed by a field, whereas that at $\mathbf{q}_3$ is enhanced, which was observed at all E studied (< 5 meV) and pronounced at 1 to ~3 meV near the edge of the SC gap (*13*). These observations are exactly what are expected for $s_\pm$-wave symmetry, implying that the sign of the SC gap is reversed between the Fermi pockets around Γ and M points, whereas adjacent M-point Fermi pockets have the same sign. With the support of the fully gapped behavior of QP density of states demonstrated in Fig. 2B, we conclude that only $s_\pm$-wave symmetry is consistent with the SI-STM data.

The sign reversal in the SC-gap function implies that the electron pairing is mediated by repulsive interaction in *k* space (*8*), which is most likely spin fluctuations associated with the nesting between the Fermi pockets (*4*–*7*). It was theoretically pointed out in models based on spin fluctuations that $s_\pm$-wave is not the only possible symmetry in iron-based superconductors; *d*-wave and nodal $s_\pm$-wave symmetries may be stabilized within the same theoretical framework, depending on the details of the band structure (*27*, *28*). Experimentally, nodal superconductivity has indeed been suggested for LaFePO and $\mathrm{BaFe_2(As_{1-x}P_x)_2}$ (*29*, *30*). It should therefore be meaningful to establish the phase structure of the SC-gap function in these materials by using the *k*-resolved phase-sensitive QPI technique to step further toward understanding the pairing mechanism of iron-based superconductors.

References and Notes

1. Y. Kamihara, T. Watanabe, M. Hirano, H. Hosono, *J. Am. Chem. Soc.* **130**, 3296 (2008).
2. Z.-A. Ren, W. Yue-Qin, Z. Li-Chun, *Chin. Phys. Lett.* **25**, 2215 (2008).
3. J. W. Lynn, P. Dai, *Physica C* **469**, 469 (2009).
4. I. I. Mazin, D. J. Singh, M. D. Johannes, M. H. Du, *Phys. Rev. Lett.* **101**, 057003 (2008).
5. K. Kuroki *et al.*, *Phys. Rev. Lett.* **101**, 087004 (2008).
6. F. Wang, H. Zhai, Y. Ran, A. Vishwanath, D.-H. Lee, *Phys. Rev. Lett.* **102**, 047005 (2009).
7. V. Cvetkovic, Z. Tesanovic, *Europhys. Lett.* **85**, 37002 (2009).
8. K. Kuroki, R. Arita, *Phys. Rev. B* **64**, 024501 (2001).
9. D. J. Singh, M.-H. Du, *Phys. Rev. Lett.* **100**, 237003 (2008).
10. K. Hashimoto *et al.*, *Phys. Rev. Lett.* **102**, 017002 (2009).
11. H. Ding *et al.*, *Europhys. Lett.* **83**, 47001 (2008).
12. T. Kondo *et al.*, *Phys. Rev. Lett.* **101**, 147003 (2008).
13. Materials and methods are available as supporting material on *Science* Online.
14. J. E. Hoffman *et al.*, *Science* **297**, 1148 (2002).
15. T. Hanaguri *et al.*, *Nat. Phys.* **3**, 865 (2007).
16. T. Hanaguri *et al.*, *Science* **323**, 923 (2009).
17. F.-C. Hsu *et al.*, *Proc. Natl. Acad. Sci. U.S.A.* **105**, 14262 (2008).
18. F. Massee *et al.*, *Phys. Rev. B* **80**, 140507 (2009).
19. T. Kato *et al.*, *Phys. Rev. B* **80**, 180507 (2009).
20. Position-dependent tip-sample separation generates an extra modulation in $g(\mathbf{r}, E)$ which predominantly has a periodicity of the underlying lattice (*31*). Unless wave function drastically changes its character in passing through the Fermi energy, such a modulation diminishes in $Z(\mathbf{r}, E)$.
21. K. Fujita *et al.*, *Phys. Rev. B* **78**, 054510 (2008).
22. T. Pereg-Barnea, M. Franz, *Phys. Rev. B* **78**, 020509 (2008).
23. M. Maltseva, P. Coleman, *Phys. Rev. B* **80**, 144514 (2009).
24. E. Plamadeala, T. Pereg-Barnea, G. Refael, http://arXiv.org/abs/0912.0527 (2009).
25. F. Wang, H. Zhai, D.-H. Lee, *Europhys. Lett.* **85**, 37005 (2009).
26. Y.-Y. Zhang *et al.*, *Phys. Rev. B* **80**, 094528 (2009).
27. S. Graser, T. A. Maier, P. J. Hirschfeld, D. J. Scalapino, *N. J. Phys.* **11**, 025016 (2009).
28. K. Kuroki, H. Usui, S. Onari, R. Arita, H. Aoki, *Phys. Rev. B* **79**, 224511 (2009).
29. J. D. Fletcher *et al.*, *Phys. Rev. Lett.* **102**, 147001 (2009).
30. K. Hashimoto *et al.*, http://arXiv.org/abs/0907.4399 (2009).
31. Y. Kohsaka *et al.*, *Science* **315**, 1380 (2007).
32. The authors thank H. Aoki, R. Arita, P. Coleman, Y. Kato, Y. Kohsaka, Y. Matsuda, I. I. Mazin, Y. Nagai, M. Ogata, T. Shibauchi, T. Shimojima, and S. Shin for valuable discussions and comments. This work has been supported by an Incentive Research Grant from RIKEN and Grant-in-Aid for Scientific Research from the Ministry of Education, Culture, Sports, Science and Technology of Japan.

Supporting Online Material
www.sciencemag.org/cgi/content/full/328/5977/474/DC1
Materials and Methods
SOM Text
Figs. S1 to S3
Tables S1 and S2
References

22 January 2010; accepted 18 March 2010
10.1126/science.1187399

Mechanism and Kinetics of Spontaneous Nanotube Growth Driven by Screw Dislocations

Stephen A. Morin,[1]* Matthew J. Bierman,[1,2]* Jonathan Tong,[1] Song Jin[1]†

Single-crystal nanotubes are commonly observed, but their formation is often not understood. We show that nanotube growth can be driven by axial screw dislocations: Self-perpetuating growth spirals enable anisotropic growth, and the dislocation strain energy overcomes the surface energy required for creating a new inner surface forming hollow tubes spontaneously. This was demonstrated through solution-grown zinc oxide nanotubes and nanowires by controlling supersaturation using a flow reactor and confirmed using microstructural characterization. The agreement between experimental growth kinetics and those predicted from fundamental crystal growth theories confirms that the growth of these nanotubes is driven by dislocations.

The question of how one-dimensional (1D) crystals grow has long fascinated scientists, starting from microscale whiskers (*1*, *2*) and continuing on to nanowires (NWs) (*3*, *4*). One-dimensional growth of NWs has been explained by the vapor-liquid-solid (VLS) mechanism (*2*, *3*) and other catalyst-driven mechanisms (*4*). The growth mechanism of frequently observed single-crystal nanotubes (NTs) (*5*) is usually thought to be unrelated to that of NWs. However, NWs can also grow via the propagation of an axial screw dislocation (*1*, *6*–*8*). Recent theoretical work has connected the growth rate of a carbon nanotube to the magnitude of the Burgers vector of a screw dislocation that it possesses (*9*). We used dislocation-driven growth to rationally grow inorganic nanotubes from solution and to explain the driving forces behind the formation of hollow tubes.

Dislocation-driven anisotropic 1D crystal growth is explained by preferred growth at the self-perpetuating spirals of axial screw disloca-

---

[1] Department of Chemistry, University of Wisconsin–Madison, 1101 University Avenue, Madison, WI 53706, USA. [2] California Institute of Technology, MC 139-74, 1200 East California Boulevard, Pasadena, CA 91125, USA.

*These authors contributed equally to this work.

†To whom correspondence should be addressed. E-mail: jin@chem.wisc.edu

tions under low supersaturations (*1*, *6*). Here, supersaturation (σ) is defined as

$$\sigma = \ln\left(\frac{c}{c_o}\right) \qquad (1)$$

where c and c_o are the concentration and equilibrium concentration of the system, respectively (*10*). According to classical crystal growth as described by the Burton-Cabrera-Frank (BCF) theory (*11*), dislocation growth, layer-by-layer (LBL) growth, and dendritic growth progressively dominate crystal growth as supersaturation is increased (fig. S1) (*10*, *11*). Therefore, intentionally exploiting low supersaturation conditions that favor the dislocation-driven growth mechanism could provide a pathway to enable catalyst-free synthesis of 1D nanomaterials. Specifically, by using flowed aqueous solutions of constant low supersaturation, we demonstrate dislocation-driven growth of single-crystal NWs and hollow NTs of zinc oxide (ZnO) in solution-phase. We show that axial screw dislocations with large magnitude contained within these materials result in the spontaneous formation of single-crystal NTs as the equilibrium morphology of 1D nanomaterials.

We chose ZnO (zincite) as a model material partly because 1D nanomaterials of semiconducting ZnO have found many applications, such as in photonics (*12*) and solar (*13*) and piezoelectronic (*14*) energy conversion, and they can be readily grown in solution (*15*, *16*). ZnO also has well-characterized dislocation microstructure (*17*). In typical aqueous synthesis, zinc salts are hydrolyzed in closed containers in the presence of weak polyamine bases, such as hexamethylenetetramine (HMT), producing ZnO NWs, nanorods (NRs) (*15*, *16*), and even NTs or microtubes (*18*, *19*). Nanostructure morphology is influenced by variations in reagent concentration, growth time, and temperature (*16*). To investigate the possibility that growth is driven by axial screw dislocations, we observe the effect of supersaturation on nanomaterial morphology and growth kinetics using the zinc nitrate and HMT reaction. However, commonly practiced closed-system hydrothermal growth of ZnO, where precursors are introduced at once and allowed to react to completion, suffers from a significant decline in the concentration of soluble zinc species during the course of the reaction (fig. S2). Such changes in the supersaturation conditions lead to irregular growth kinetics that are difficult to deconvolute and may affect morphology. We therefore developed a continuous flow reactor (CFR) (fig. S3) (*20*) to maintain constant supersaturation and enable indefinite reaction times.

We observed a dramatic morphology dependence of the growth products on supersaturation. Specifically, when CFR experiments are run at decreasing precursor concentrations from millimolar (mM) down to micromolar (μM) (*20*), a steady decrease in diameter and an increase in aspect ratio of the resulting 1D ZnO nanomaterials is observed (Fig. 1, A to C). High concentrations (10 mM) yield NRs of about 270 nm in diameter with clear tapering (Fig. 1A), rather similar to what are observed in closed-system growth (fig. S11E). Intermediate concentrations (500 μM) produce NWs of about 100 nm in diameter (Fig. 1B), and the lowest concentrations (30 μM) yield high-aspect-ratio nanostructures of about 22 nm in diameter (Fig. 1, C to F). These nanomaterials were confirmed to be of the single-crystal wurtzite structure with growth along the [001] direction by transmission electron microscopy (TEM) (Fig. 1, D and F; only data for low-concentration NWs shown) and electron diffraction (ED) (Fig. 1E, inset). In all cases, seed nuclei were first created in a separate high-concentration (100 mM) nucleation step (*20*). This is important for the extremely low-concentration reactions (Fig. 1, C to E) that are below the concentration necessary for heterogeneous nucleation. Occasionally, these seeds are visible at the bases of NWs synthesized at the lowest concentration (Fig. 1F). Interestingly, they have a coherent crystal lattice with the NWs but contain more

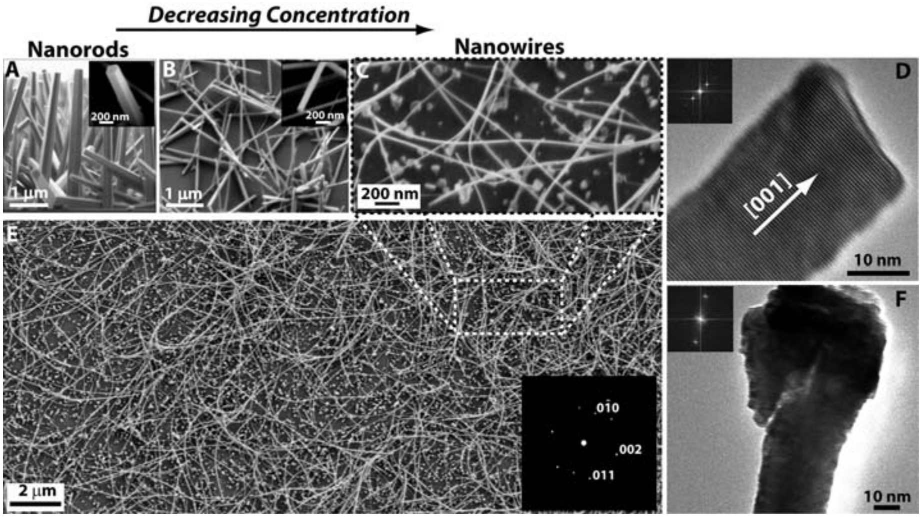

Fig. 1. Evolution of ZnO morphology with decreasing precursor concentration (supersaturation). Scanning electron micrographs of ZnO morphology evolution, from NRs/NWs (**A** and **B**, run at concentrations of 10 mM and 500 μM, respectively) to high-aspect-ratio ZnO NWs (**C** and **E**, run at 30 μM), as supersaturation is decreased in the CFR. The electron diffraction pattern along [100] zone axis [inset in (E)] confirms that the NWs are zincite. The NWs (E) grow along the [001] direction as indicated by high-resolution TEM (**D**) and form continuous crystals with the seed nuclei as shown in TEM (**F**). The corresponding fast Fourier transform images are shown in the (D) and (F) insets.

Fig. 2. TEM observation of screw dislocations within ZnO NWs and the crystal behavior of NTs. Several TEM images of a ZnO NW are tiled together to provide perspective of the areas examined (**A**). Exciting the (002) spot in the [100] zone axis pattern (ZAP) shows dislocation contrast (**B**), whereas exciting the orthogonal (010) spots makes the dislocation invisible (**C**). Because both the growth direction and dislocation direction are along [001], this behavior is consistent with a dislocation of screw character. The amorphous coating in (A) to (C) is carbon deposition from the TEM. Several micrographs succinctly show the variety of possible morphologies, including solid NWs (**D**), the intermediate voided NWs (**E** and **F**), and the hollow NT (**G**), whose forms are dictated by the strength of the dislocation (Burgers vector magnitude). Two cases are shown where the voids are either irregularly (E) or evenly (F) spaced. All images share a 50-nm scale bar except (A).

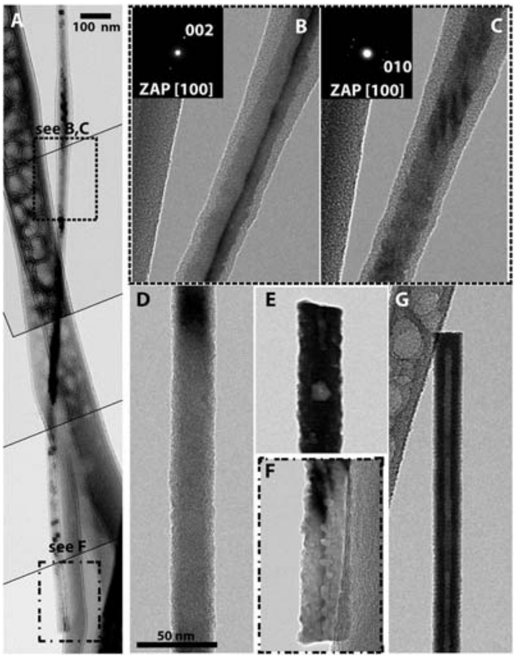

defects. These defects suggest slight misorientation between adjacent crystal grains that form each seed nuclei and presumably provide a source for dislocations (*21*). Such dislocations could then propagate the NW growth.

We observed axial dislocations in the thin, high-aspect-ratio NWs grown at low concentrations (Fig. 1, C to F) using diffraction contrast TEM. For diffraction contrast images taken along the [100] zone axis (Fig. 2, B and C), dislocation contrast is visible under the two-beam condition that excites the (002) diffraction spot (Fig. 2B), which is along the direction of the dislocation line and NW growth axis. Exciting the orthogonal (010) family of spots, the dislocation becomes invisible (Fig. 2C), consistent with the behavior of a screw dislocation.

Nearly all the products from low-concentration CFR synthesis examined under TEM were not NWs with solid cores such as the one shown in Fig. 2D, but instead voided (Fig. 2, E and F) or hollow NTs (Fig. 2G). Axial screw dislocations contained within NWs not only drive anisotropic growth but also cause the spontaneous formation of NTs due to the dislocation strain energy. Because of the disruption of the perfect periodicity within the crystal lattice, there is a strain energy per unit length (E) due to a screw dislocation that is quadratically dependent on the magnitude of the Burgers vector (b)

$$E = \frac{b^2\mu}{4\pi}\ln\left(\frac{R}{r}\right) \qquad (2)$$

where μ is the shear modulus, and R and r are the outer and inner tube radii, respectively (*22*, *23*). As b increases, eventually the crystal contains enough strain energy that it exceeds the energy cost of creating a new inner surface and the dislocation core becomes hollow. This causes the formation of micropipes often observed in dislocation-prone materials such as SiC or GaN (*22*, *24*). An energy balance between surface energy ($2\pi\gamma r$, where γ is surface energy) and the strain energy from Eq. 2 (both per unit length) results in a relationship between r and b (*22*).

$$b_{TUBE} = \sqrt{\frac{8\pi^2\gamma r}{\mu}} \qquad (3)$$

For NWs reaching this energy threshold, the solid NW becomes a hollow NT, as observed in these ZnO nanostructures (Fig. 2, D to G). Essentially, the equilibrium morphology of 1D nanomaterials whose growth is driven by screw dislocations should be hollow NTs (Fig. 3A) when the Burgers vector is sufficiently large (*25*). It is possible that the intermediate (void) case is on the threshold and oscillates between the solid and hollow conditions due to small fluctuations in growth environment and NW thickness that subtly change the energy balance, or tubes initially formed could partially close up after synthesis.

The strain energy imbalance due to a coaxial screw dislocation in a cylinder also results in a torque around the dislocation known as the Eshelby twist (*26*). This was confirmed in nanowire pine trees of PbS and PbSe (*6*, *7*). For tubes, the Eshelby twist equation must be modified (*27*) from the solid cylinder case to

$$\alpha = \frac{b}{\pi R^2 + \pi r^2} \qquad (4)$$

with α representing lattice twist in radians/length and R and r representing the outer and inner radii of the tube, respectively. Attempts to observe the twist in these ZnO NTs by indexing the zone axis via electron diffraction as the electron beam is moved along the object revealed no Eshelby twist above the detection limits of the technique, which is about 5° of absolute twist (fig. S4) (*20*). We further adopted a finer technique (*28*) of indexing twist contours using dark field TEM (fig. S5) that allowed the estimate of a twist of ~1.6°/μm for these completely hollow thin NTs and ~ 4.5°/μm for solid NWs with larger diameter (~100 nm). Although the amount of twist observed in the larger-diameter solid NWs is in line with the Eshelby prediction, such a small amount of twist in the small diameter NTs was puzzling because Eq. 4 predicts twists of ~100°/μm. This made us realize that the classic dislocation micropipe treatment by Frank was incomplete for 1D NTs because it overlooks the Eshelby twist mechanism for strain energy relief. The very small Eshelby twist in NTs is expected if we consider that there are two competing mechanisms for the alleviation of dislocation strain: (i) forming a hollow core and (ii) producing a torque around the dislocation axis via the Eshelby twist mechanism.

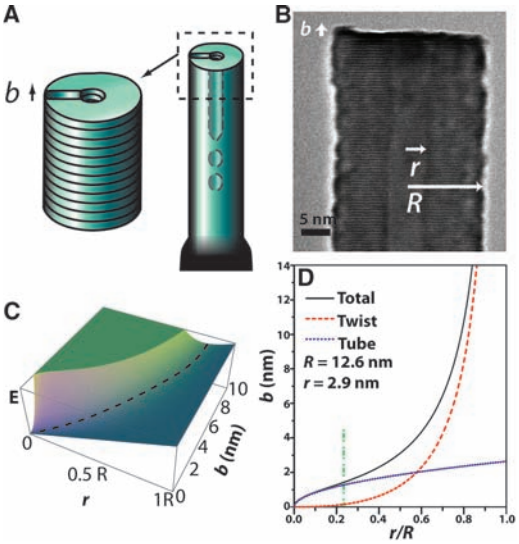

Fig. 3. Two pathways to relieve the strain energy and the estimation of b in ZnO NTs. Large strain energy contained within a screw dislocation coaxial to a nanowire leads to the formation of a NT or voided structure as schematically illustrated (**A**). A HRTEM of the tip of a NT (**B**) allows direct measurement of the critical parameters R, r, and b. The energy for a dislocated ZnO NT (**C**) is shown from Eq. 5 to be dependent on r and b for fixed R. The dashed line represents the energy minimum. By explicitly solving Eq. 5 along this energy valley, we obtain an energy-minimized relation for b versus r/R (**D**) for the specific ZnO NT in (B), where R = 12.6 nm, r = 2.9 nm, and b = 1.9 nm [r/R = 0.23, noted by the vertical green line in (D)]. The total contribution to b (Eq. 6) has components due to the hollow inner tube surface energy (Tube) and to the Eshelby twist (Twist). At low Burgers vector, the total effect follows the dislocation hollow core line and almost all strain energy is alleviated by hollowing out the dislocation core. At larger Burgers vector and larger inner core radius, the surface energy becomes large and all new strain energy is relaxed through the Eshelby twist, with the intermediate b transitioning between these two limits.

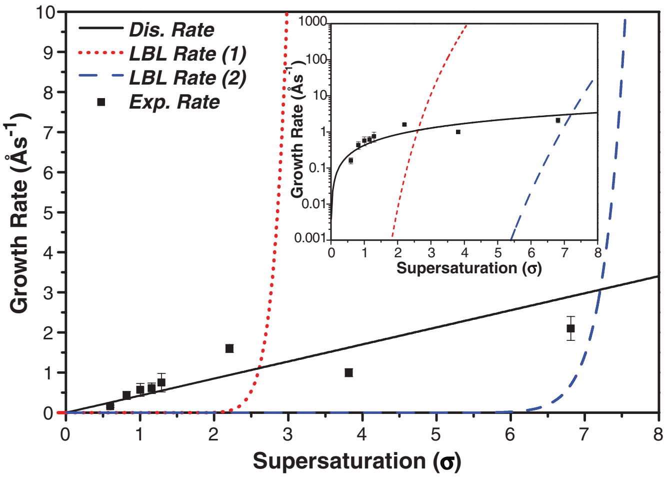

Fig. 4. Summary of experimental and theoretical ZnO crystal growth kinetics. Theoretical growth rates as a function of supersaturation for a dislocation mechanism (solid) and LBL mechanism calculated using a c_0 of 11 μM and physical constants (small dashed line uses a small surface energy value of 0.16 J/m2; large dashed line uses an intermediate surface energy value of 0.31 J/m2) for growth along the c axis of ZnO. Experimental growth rates (squares; error bars show SD) clearly follow the trend predicted by a dislocation mechanism. This is further illustrated by the logarithmic rate plot (inset).

Once the nanostructure becomes hollow, the overall energy per unit length (E) contains three terms: the surface energy from the hollow inner tube, the lattice strain due to the dislocation, and the reduction in lattice strain due to the Eshelby twist.

$$E = 2\pi\gamma r + \frac{\mu b^2}{4\pi}\ln\left(\frac{R}{r}\right) - \frac{\mu b^2}{4\pi}\frac{(R^2 - r^2)}{(R^2 + r^2)} \quad (5)$$

Using ZnO specific values for surface energy, 0.31 J/m^2 (*20*), shear modulus, 44.3 GPa (*29*), and the radii of the NT shown in Fig. 3B allows for an evaluation of this equation. A 3D surface plot of Eq. 5 constructed for E versus b and r/R (Fig. 3C) shows that there is an energy valley (minimum) associated with certain optimized r and b values (marked with a dashed line). The energy-minimized relation between r and b can be solved by setting the energy derivative with respect to r to zero.

$$\frac{dE}{dr} = 0 \rightarrow b_{\mathrm{TOTAL}} = \sqrt{\frac{8\pi^2\gamma r}{\mu}\left(\frac{R^2 + r^2}{R^2 - r^2}\right)} \quad (6)$$

The first factor in Eq. 6 represents the effect from Frank's hollow-tube mechanism (see Eq. 3) (*22*), whereas the second factor is the modification due to the Eshelby-twist pathway. The Eshelby-twist component can also be expressed explicitly as the difference between Eq. 6 and Eq. 3.

$$b_{\mathrm{TWIST}} = b_{\mathrm{TOTAL}} - b_{\mathrm{TUBE}} = \sqrt{\frac{8\pi^2\gamma r}{\mu}}\left(\sqrt{\frac{R^2 + r^2}{R^2 - r^2}} - 1\right) \quad (7)$$

This direct relation between the r and b variables along the energy valley (Eq. 6 and dashed line in Fig. 3C) contains the contributions to the total energy from the Eshelby-twist and hollow-tube components and can be alternately displayed as a plot of b versus r/R (Fig. 3D). At low b, the total energy minimization approximates the Frank hollow-tube mechanism, and most energy is relieved by making the tube hollow. However, at much larger b (and larger r), the total energy minimization begins to follow the Eshelby-twist line. That is, as the NT becomes a cylindrical shell, creating more surface becomes energetically forbidden, and most energy goes toward the Eshelby twist. For the ZnO NT in Fig. 3B, the vertical dashed line (r/R = 12.6 nm/2.9 nm = 0.23) in Fig. 3D predicts that this tube follows the former limit, and the strain energy is alleviated almost purely by hollowing out into a NT, consistent with our observation of very little Eshelby twist in ZnO NTs.

So what then is the Burgers vector magnitude (b) for these ZnO NTs? Burgers vector magnitudes are generally difficult to determine. Following scanning probe microscopy techniques that measure the growth spiral step height around the screw dislocation core as b (*24*, *30*), we suggest a measurement of the step height from the tip of NTs using high-resolution TEM (HRTEM) (Fig. 3B and fig. S7). Because LBL growth is expected to be virtually shut off under these conditions, this step edge is unlikely the result of a nucleated island. For NTs that show clear c-axis planes, the distance between the highest lattice fringe and the last lattice fringe that is continuous throughout the NT can be approximated as b, which is about 1.9 nm for this representative NT (Fig. 3B). Alternatively, from dislocation energy minimization (Eq. 6) we can directly estimate the b to be 1.4 nm for the same NT (R = 12.6 nm and r = 2.9 nm). Despite the limitations of both approximations, they give similar estimates.

To prove that the growth of ZnO NWs, NTs, and thicker NRs containing axial screw dislocations (for evidence of axial dislocations in NRs, see fig. S11) is driven by dislocations, we compare experimentally determined growth kinetics with those predicted using fundamental BCF (*10*, *11*) and LBL crystal growth theories (*10*). Thorough treatment of both crystal growth theories in detail can be found in the supporting online material (*20*). Briefly, BCF theory predicts a dislocation-growth rate ($R_{\mathrm{disloction}}$) linearly dependent on supersaturation

$$R_{\mathrm{dislocation}} = C\sigma \quad (8)$$

where the rate constant C can be calculated (*10*, *11*, *20*). In contrast, LBL growth has an exponential growth rate (R_{lbl})

$$R_{\mathrm{lbl}} = J_{\mathrm{o}}L^2\beta \propto e^{\left(-\frac{g_{\mathrm{n}}}{kT}\right)}L^2\beta \quad (9)$$

where J_{o} is the rate of 2D nucleation, L is the length of the facet (assuming a square growth facet), β is the step height, k is Boltzmanns constant, T is the temperature, and g_{n} is the energy barrier to 2D nucleation, which is inversely proportional to supersaturation (*20*). These expressions illustrate that, although LBL growth requires the formation of 2D nuclei by overcoming the energy barrier g_{n}, dislocation growth has no such barrier because of self-perpetuating growth steps; therefore, at low supersaturations dislocation growth dominates. Only at supersaturations above the critical supersaturation of forming 2D nuclei is LBL expected to overtake dislocation growth (fig. S1). These macroscopic growth rates for dislocation (Eq. 8) and LBL (Eq. 9) growth are plotted as a function of supersaturation for ZnO growth using appropriate parameters (Fig. 4) (*20*).

We have determined experimental axial growth rates by conducting a series of growth experiments over a range of precursor concentrations (c) from 20 μM to 10 mM and surveying the lengths of the NR/NW/NT products (fig. S9) (*20*). These experimental growth rates are plotted as a function of supersaturation (σ) against those theoretically predicted (Fig. 4). To convert c to σ using Eq. 1, we empirically determine the equilibrium concentration (c_{o}) to be 11 μM by finding the concentration at which the initial ZnO seed crystals are stable, that is, neither dissolving nor growing into NWs (fig. S8) (*20*). It is clear that the experimentally measured ZnO NR/NW/NT growth rates follow the rate law predicted by dislocation-driven growth and not that predicted by LBL growth. Because a single value of specific surface energy for ZnO, which heavily influences g_{n}, has not been reported, LBL growth rates calculated using a conservative value of 0.16 J/m^2 and an intermediate value of 0.31 J/m^2 (among the reported surface energy range of 0.1 to 0.7 J/m^2) are displayed in Fig. 4. For all calculations, experimental growth rates do not follow the LBL model. Although the apparent good match between experimental and theoretical dislocation growth rates might be incidental, the logarithmic growth rate plot (inset of Fig. 4) shows that the dislocation and LBL growth rate trends are so different that even errors of several orders of magnitude would not support a different conclusion. Together with the observation of axial dislocations and NT formation, this proves that the solution growth of ZnO NRs, NWs, and NTs in various concentration regimes, observed by us or reported in the literature, is indeed driven by dislocations. Furthermore, the observed decrease in aspect ratio with increasing supersaturation (Fig. 1, C to A) may be explained by the competition between dislocation and LBL growth mechanisms at different supersaturations (fig. S10) (*20*). Because only axial dislocations are observed, LBL growth accounts for radial growth (broadening) exclusively, and the barrier to 2D nucleation on the side walls heavily impacts aspect ratio. Supersaturations below this barrier yield high-aspect-ratio NWs/NTs; those above it do not (fig. S10, C and D).

We have shown that large axial screw dislocations in NWs result in the spontaneous formation of single-crystal NTs as the equilibrium morphology and explained why thick-walled dislocated NTs have very little Eshelby twist. The growth kinetics of these materials follow the prediction of the dislocation growth mechanism as described by BCF theory, confirming that axial screw dislocations seen in these materials drive the anisotropic growth of NWs or NTs. The connections between supersaturation, preferred crystal growth mechanism, energetics of dislocations, and the final morphology elucidated here present unifying concepts to explain and control the variety of 1D nanomaterial morphologies (NR, NW, and NT) reported. Although ZnO is used as a specific example herein, we provide a general theoretical framework for controlling solution NW/NT growth that can be applied to other materials.

References and Notes

1. G. W. Sears, *Acta Metall.* **3**, 361 (1955).
2. R. S. Wagner, W. C. Ellis, *Appl. Phys. Lett.* **4**, 89 (1964).
3. A. M. Morales, C. M. Lieber, *Science* **279**, 208 (1998).
4. Y. N. Xia *et al.*, *Adv. Mater.* **15**, 353 (2003).
5. G. R. Patzke, F. Krumeich, R. Nesper, *Angew. Chem. Int. Ed.* **41**, 2446 (2002).

6. M. J. Bierman, Y. K. A. Lau, A. V. Kvit, A. L. Schmitt, S. Jin, *Science* **320**, 1060 (2008).
7. J. Zhu *et al.*, *Nat. Nanotechnol.* **3**, 477 (2008).
8. Y. K. A. Lau, D. J. Chernak, M. J. Bierman, S. Jin, *J. Am. Chem. Soc.* **131**, 16461 (2009).
9. F. Ding, A. R. Harutyunyan, B. I. Yakobson, *Proc. Natl. Acad. Sci. U.S.A.* **106**, 2506 (2009).
10. I. V. Markov, *Crystal Growth For Beginners: Fundamentals of Nucleation, Crystal Growth, and Epitaxy* (World Scientific Publishing, Singapore, ed. 1, 1995).
11. W. K. Burton, N. Cabrera, C. Frank, *Philos. Trans. R. Soc. London Ser. A* **243**, 299 (1951).
12. M. H. Huang *et al.*, *Science* **292**, 1897 (2001).
13. M. Law, L. E. Greene, J. C. Johnson, R. Saykally, P. D. Yang, *Nat. Mater.* **4**, 455 (2005).
14. Z. L. Wang, J. H. Song, *Science* **312**, 242 (2006).
15. L. Vayssieres, K. Keis, S. E. Lindquist, A. Hagfeldt, *J. Phys. Chem. B* **105**, 3350 (2001).
16. K. Govender, D. S. Boyle, P. B. Kenway, P. O'Brien, *J. Mater. Chem.* **14**, 2575 (2004).
17. G. Dhanaraj, M. Dudley, D. Bliss, M. Callahan, M. Harris, *J. Cryst. Growth* **297**, 74 (2006).
18. Y. Sun, G. M. Fuge, N. A. Fox, D. J. Riley, M. N. R. Ashfold, *Adv. Mater.* **17**, 2477 (2005).
19. Q. C. Li *et al.*, *Chem. Mater.* **17**, 1001 (2005).
20. Materials, methods, and detailed discussion of crystal growth theory and rate calculations are available as supporting material on *Science* Online.
21. R. L. Penn, J. F. Banfield, *Science* **281**, 969 (1998).
22. F. C. Frank, *Acta Crystallogr.* **4**, 497 (1951).
23. F. R. N. Nabarro, *Theory of Crystal Dislocations* (Oxford, London, 1967).
24. J. Heindl, H. P. Strunk, V. D. Heydemann, G. Pensl, *Phys. Status Solidi A* **162**, 251 (1997).
25. It is likely that this energy balance causes the material to grow directly as a tube with the self-perpetuating steps driving elongation (Fig. 3A), although first growing as a wire and becoming hollow after synthesis could also happen if there is a sufficient change in surface energy that shifts the energy balance after synthesis (during cooling, for instance). Although it has been shown by Frank that micropipe formation often occurs for a single dislocation with a Burgers vector exceeding 1 nm, it is also possible to exceed this energy by the action of *n* parallel dislocations, each of a common magnitude. Again, Frank has shown the stability of essentially any number of parallel screw dislocations with the same handedness in a 1D whisker. In cases where one dislocation is of opposite handedness, this dislocation is forced out of the crystal by the action of the dislocations of opposite sign. In terms of energy, multiple dislocations have a total energy that is additive ($E_{\mathrm{Total}} = nE$), whereas a single dislocation has an energy that is larger ($E_{\mathrm{Total}} = n^2E$), where *n* is the number of "primary" dislocations. Therefore, a NW containing a single large *b* dislocation will more quickly favor tube growth than one containing multiple dislocations. Considering that NTs are the dominate morphology for the CFR grown materials and that we have not observed any evidence of multiple parallel dislocations so far, we believe single large *b* axial dislocations exist in these NWs/NTs.
26. J. D. Eshelby, *J. Appl. Phys.* **24**, 176 (1953).
27. J. D. Eshelby, *Philos. Mag.* **3**, 440 (1958).
28. C. M. Drum, *J. Appl. Phys.* **36**, 824 (1965).
29. T. B. Bateman, *J. Appl. Phys.* **33**, 3309 (1962).
30. H. H. Teng, P. M. Dove, J. J. De Yoreo, *Geochim. Cosmochim. Acta* **64**, 2255 (2000).

31. S.J. thanks NSF (CAREER DMR-0548232), UW-Madison NSEC (NSF DMR 0425880 and 0832760), Research Corporation Cottrell Scholar Award, DuPont Young Professor Grant, and Sloan Research Fellowship for support. S.A.M. was partially supported by a 3M Graduate Research Fellowship.

Supporting Online Material

www.sciencemag.org/cgi/content/full/328/5977/476/DC1
Materials and Methods
Figs. S1 to S11
Table S1
References

7 October 2009; accepted 2 March 2010
10.1126/science.1182977

Monolithic Carbide-Derived Carbon Films for Micro-Supercapacitors

John Chmiola,[1]* Celine Largeot,[2] Pierre-Louis Taberna,[2] Patrice Simon,[2] Yury Gogotsi[1]†

Microbatteries with dimensions of tens to hundreds of micrometers that are produced by common microfabrication techniques are poised to provide integration of power sources onto electronic devices, but they still suffer from poor cycle lifetime, as well as power and temperature range of operation issues that are alleviated with the use of supercapacitors. There have been a few reports on thin-film and other micro-supercapacitors, but they are either too thin to provide sufficient energy or the technology is not scalable. By etching supercapacitor electrodes into conductive titanium carbide substrates, we demonstrate that monolithic carbon films lead to a volumetric capacity exceeding that of micro- and macroscale supercapacitors reported thus far, by a factor of 2. This study also provides the framework for integration of high-performance micro-supercapacitors onto a variety of devices.

Microbatteries with the capability to be fabricated with length scales controlled in the micrometer range improve performance over their larger cousins by decreasing diffusion lengths, increasing the fraction of electroactive materials and making use of precise fabrication protocols. The prospect of integrating microbatteries as discrete power sources with the micro-electromechanical systems (MEMS), the devices they power, and the capacity for autonomous recharging represents a conceptual leap forward over existing methods for powering devices. This could potentially increase the density of devices allowing improved functionality, reduced complexity, and enhanced redundancy by removing intricate interconnects to bulk-sized batteries. Currently, advanced rechargeable microbatteries that use thin-film technologies are commercially available (*1*), but they suffer from many of the limitations of their larger counterparts, namely limited cycle life, abrupt failure, poor low-temperature kinetics, and safety concerns associated with using lithium (*2*). Even three-dimensional (3D) batteries (*1*), which are expected to overcome power limitations by further shortening electrolyte path lengths, cannot avoid fast failure because of the inevitable self-discharge caused by electron tunneling through marginally conductive thin dielectric coatings (solid electrolytes) and repeated recharging cycles. Electrochemical capacitors (ECs), also called ultracapacitors or supercapacitors, can solve these lifetime and power issues and provide a bridge between devices operating with short charge-discharge times (<0.1 s) and longer discharge times (>0.1 hours) under and over which dielectric or electrolytic capacitors and batteries, respectively, find their niche (*3*). However, compared to lithium-ion batteries, very little work has been done to integrate ECs on a chip or to produce thin- and thick-film ECs in general.

The power density and cycle time of ECs enable them to improve the efficiency of a battery when the two are used together (*4*). ECs can harvest the excess kinetic energy, such as in the braking of a motor vehicle or the vibrations of a moving object. ECs store energy through reversible ion adsorption at the surface of high–specific surface area carbons at the carbon-electrolyte interface, in a so-called double-layer (*3*), whereas batteries store electrical energy in chemical bonds in a bulk material (*5*, *6*). ECs do not require slow charge or discharge to satisfy relatively sluggish electrochemical charge-transfer kinetics that maintain the thermodynamic steady state in batteries. Additionally, because only physical motion of charge carriers dictates the charge stored (*7*), they can handle currents that are larger by several orders of magnitude (*8*). Moreover, because EC electrostatics avoids battery and fuel-cell chemical kinetics, EC efficiency and reversibility exceed 90%, even at very high discharge rates (*4*). In combination with a practically infinite cycle life, ECs seem ideal for capturing and storing energy from renewable resources and for on-chip operation.

There have been notable advances in the micro-supercapacitor field, which were mostly focused on increasing micro-supercapacitor energy density by using different active materials (*9*) and designs, such as carbon nanotubes (CNTs) (*10*, *11*), activated carbons (*12*), polymers (*13*),

---

[1] Department of Materials Science and Engineering and A. J. Drexel Nanotechnology Institute, Drexel University, Philadelphia, PA 19104, USA. [2] Université Paul Sabatier de Toulouse, Inter-University Research and Engineering Center on Materials (CIRIMAT), UMR-CNRS 5085, 31062 Toulouse Cedex 4, France.

*Present address: Environmental Energy Technologies Division, Lawrence Berkeley National Laboratory, Berkeley, CA 94720, USA.

†To whom correspondence should be addressed. E-mail: gogotsi@drexel.edu